

Article

Pt₂ Dimer Anchored Vertically in Defective BN Monolayer as an Efficient Catalyst for N₂ Reduction: A DFT Study

Linke Yu and Fengyu Li * 

Physical School of Science and Technology, Inner Mongolia University, Hohhot 010021, China

* Correspondence: fengyuli@imu.edu.cn

Abstract: The electrochemical nitrogen reduction reaction (NRR) using clean energy is considered a promising alternative to the conventional Haber–Bosch process; however, developing a highly active electrocatalyst is still a great challenge. In this study, ten metal dimers anchored in a defective boron nitride (BN) monolayer as double-atom catalysts (DACs) with reverse sandwich structures were screened for their stability and catalytic activity towards NRR by density functional theory (DFT) calculations. Among them, three DACs (Rh₂⊥vb-BN, Pt₂⊥vb-BN and Rh₂⊥vn-BN) were confirmed to be stable and have high promise as NRR electrocatalysts, and Pt₂⊥vb-BN particularly distinguishes itself due to its very low limiting potential (−0.06 V). In addition, the electrocatalytic performance of all three DACs prevailed over that of their single-atom catalyst counterparts. We believe that the unique conformation of the reverse sandwich structure has impressive potential for the development of DACs, and we hope that our study provides a new design strategy for DACs for NRR and beyond.

Keywords: nitrogen reduction reaction; double-atom catalysts; reverse sandwich structure; metal dimer; boron nitride monolayer; density functional theory



Citation: Yu, L.; Li, F. Pt₂ Dimer Anchored Vertically in Defective BN Monolayer as an Efficient Catalyst for N₂ Reduction: A DFT Study. *Catalysts* **2022**, *12*, 1387. <https://doi.org/10.3390/catal12111387>

Academic Editors:
Guillermo Ahumada and
Jonathan Cisterna

Received: 14 October 2022
Accepted: 7 November 2022
Published: 8 November 2022

Publisher's Note: MDPI stays neutral with regard to jurisdictional claims in published maps and institutional affiliations.



Copyright: © 2022 by the authors. Licensee MDPI, Basel, Switzerland. This article is an open access article distributed under the terms and conditions of the Creative Commons Attribution (CC BY) license (<https://creativecommons.org/licenses/by/4.0/>).

1. Introduction

Ammonia (NH₃) has always been an indispensable substance for industry and agriculture [1,2]. In contrast, nitrogen, an element present in the Earth's atmosphere in the form of nitrogen gas (N₂), is not metabolized by most living organisms [3,4]. Therefore, the direct reduction of N₂ to ammonia (NH₃) is one of the most important but challenging chemical transformations [5]. Although humans have mastered the process of large-scale ammonia synthesis for nearly a century, the traditional Haber–Bosch process has so far been relied upon primarily to produce ammonia; however, the Haber–Bosch process requires harsh reaction conditions, including high pressures and temperatures, indicating high energy consumption [6–8]. Therefore, finding economical and environmentally friendly nitrogen fixation routes as an alternative strategy to the Haber–Bosch process is essential.

Electrocatalytic nitrogen fixation using clean energy is a promising alternative approach due to its mild reaction conditions [9]. Therefore, it is crucial to design efficient electrocatalysts for the electrochemical conversion of N₂ to NH₃ under mild conditions [10]. To date, many catalysts have been utilized to catalyze nitrogen reduction reactions (NRRs), including transition metals (e.g., Fe, Co, Mo and Pt), transition metal alloys, nitrides, oxides, carbides, borides, etc. [11–15]. Since the proposal of single-atom catalysts in 2011 [16], such single- and double-atom catalysts (SACs/DACs) loaded on two-dimensional materials have received widespread attention not only for their capability to maximize metal utilization but also for their high activity and selectivity [17–19]. Various SACs and multi-atom catalysts have been designed as electrocatalysts for nitrogen reduction, such as Fe@NC [20], Pt-C₃N₄ [21], Mo-BN [22], M₂-Pc [5], Fe₃@C₂N [23], Ru₂@GY [24], etc.

With the development of experimental techniques, appropriate substrates are crucial for the immobilization of single (double) metal atom(s). Among them, hexagonal boron

nitride (*h*-BN) sheets have attracted the interest of researchers due to their honeycomb lattice morphology, similar to that of graphene [25,26]. Unlike graphene, the B–N bonds in *h*-BN sheets have a polar nature, and they have superior thermal and chemical stability, high thermal conductivity, superior optoelectronic properties and good oxidation resistance [27–29]. Although *h*-BN has a wide band gap (~6 eV), suitable for by doping metals, *h*-BN can be transformed into a semiconductor or turned into a metal to be used in electrocatalysis, such as the oxygen reduction reaction [30,31], the nitrogen reduction reaction [22,32], the carbon dioxide reduction reaction (CO₂RR) [33,34] and methane oxidation [35]. Using DFT calculations, Zhao and Chen demonstrated that single Mo atoms supported by a defective boron nitride nanosheet exhibit very high catalytic activity for N₂ immobilization through an enzymatic mechanism with a limiting potential of –0.35 V [22]. Zhou and coworkers revealed that embedding double metal atoms in defective *h*-BN can completely modify *h*-BN to metal and exhibit excellent catalytic performance for CO₂RR [33].

Very recently, we theoretically designed a few metal dimers anchored perpendicularly in defective graphene forming an inverse sandwich structure (M₂⊥gra, M = Co, Ni, Rh, Ir and Pt), and the computations indicated that these DACs have reasonable stabilities and are promising gas sensors due to the alternation of electronic and magnetic properties upon gas adsorption [36]. Moreover, such structures show superior catalytic capability for CO₂RR: the limiting potentials of RhIr⊥gra and RhPt⊥gra are –0.36 and –0.26 V, respectively [37]. Therefore, it is natural to ask whether such reverse sandwich structures can be achieved in other two-dimensional materials and whether these reverse sandwich structures be used as electrocatalysts for NRR. To answer these questions, we designed ten BN-based DACs with reverse sandwich structures and explored their stability and potential for NRR.

In this work, density functional theory (DFT) calculations were performed to systematically investigate the electrocatalytic performance of 10 DACs, M₂⊥vb-BN (M = Co, Ni, Rh, Ir, and Pt) and M₂⊥vn-BN (M = Co, Ni, Rh, Ir, and Pt), for NRR, where M₂⊥vb-BN (M₂⊥vn-BN) denotes a metal dimer vertically embedded in the B(N)-vacancy of a BN monolayer (Figure 1). Our computations show that Pt₂⊥vb-BN is a rather efficient NRR electrocatalyst with a limiting potential of only –0.06 V. We also compared the electrocatalytic performance of three promising DACs (Rh₂⊥vb-BN, Pt₂⊥vb-BN and Rh₂⊥vn-BN) with that of their single-atom catalysts (Rh@vb-BN, Pt@vb-BN and Rh@vn-BN) and found that all of the DACs with reverse sandwich structures outperformed the SACs. Our work reveals the promise of metal dimers loaded perpendicularly in defective *h*-BN, i.e., inverse sandwich structures, as electrocatalysts for NRR, thus providing a novel design scheme for double-atom catalysts.

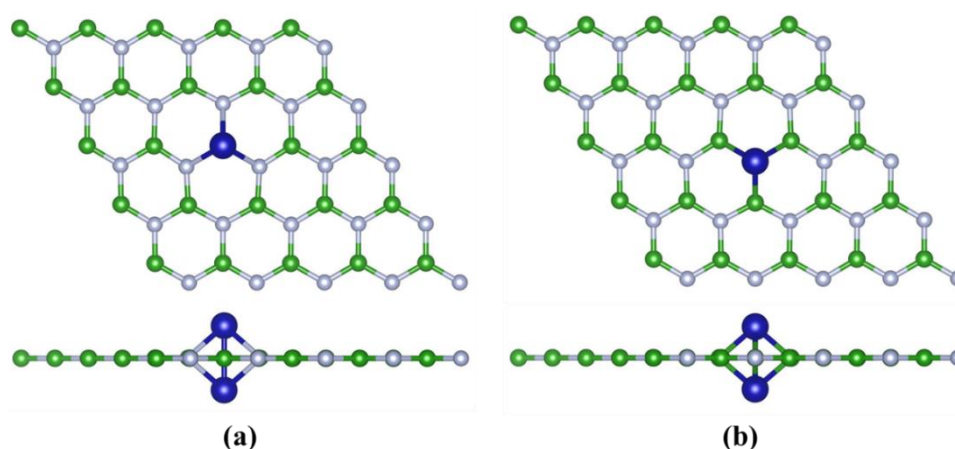


Figure 1. Structural diagram of the (a) M₂⊥vb-BN and (b) M₂⊥vn-BN models. Color scheme: B, green; N, silver; M, blue.

2. Results and Discussion

2.1. The Stability, Magnetic and Electronic Properties of DACs

We first calculated the single-cell structure of *h*-BN with a cell size of 2.52 Å and a B-N bond length of 1.45 Å, as shown in Figure S1a, which is the same as in the previous study [38]. In our study, two defective configurations of a boron atom vacancy (vb-BN) and a nitrogen atom vacancy (vn-BN) were constructed using a 5 × 5 *h*-BN supercell, as shown in Figure S1b,c. As shown in Figure 1, two transition-metal M atoms are symmetrically located at the top and bottom of the vacancy of *h*-BN; each metal M atom is bound to three nitrogen or boron atoms, respectively, and two M atoms are also bound to each other, forming M₂⊥vb-BN and M₂⊥vn-BN configurations with an inverse sandwich structure (Figure 1). The distances between metal atoms (*D*) are listed in Table S1. The distances between metal atoms are all within 3 Å, indicating good bonding between metals, except that the *D* of Ir₂ is larger than 3 Å, which might be attributable to the instability of Ir₂⊥vn-BN, as discussed afterwards. We demonstrated in our previous study that five transition metals (M = Co, Ni, Rh, Ir and Pt) can be stably embedded vertically in defective graphene, so we proceeded to evaluate their stability in the M₂⊥vb-BN and M₂⊥vn-BN configurations [36].

First, using Equation (1) (see Section 3), we calculated the binding energy (E_b) for the 10 structures on defective *h*-BN and compared it with the cohesion energy ($E_{coh} = (E_{bulk} - nE_M)/n$, where E_M and E_{bulk} are the energies of a free M atom and the total energy of the M bulk, respectively, and n is the number of M atoms) in the bulk phase of the corresponding metal. If $\Delta E = E_b - E_{coh}$ is less than or close to zero, these systems are thermodynamically stable [39]. The results are listed in Table S1. Ir₂⊥vb-BN and Ir₂⊥vn-BN are unstable due to their large ΔE and are not considered in the subsequent discussion.

Next, first-principles molecular dynamics (FPMD) simulations were performed to evaluate the thermal stability of the remaining eight catalysts. Fortunately, during the molecular dynamics simulations at room temperature (300 K) with a time step of 1 fs and a time duration of 5 ps, the structures of all eight catalysts were well preserved with slight energy vibrations (Figure S2), demonstrating that they were all stable at room temperature. Therefore, we screened the eight stable DACs (M₂⊥vb-BN and M₂⊥vn-BN; M = Co, Ni, Rh and Pt) for further study.

Then, we explored the magnetic and electronic properties of the eight stable DACs. Their Bader charges and magnetic properties are summarized in Table S2. In the four DACs with B-vacancy, the metal atoms (Co, Ni, Rh and Pt) all lose electrons, and the upper and lower metal atoms carry the same charge (+0.84, +0.76, +0.50 and +0.44 |e|); in the four DACs with N-vacancy, because the metal atoms are bonded to the B atoms, not all of the metal atoms (Co) lose electrons: three types of metal atoms (Ni, Rh and Pt) gain electrons to show a negative charge, and again, the upper and lower metal atoms carry the same charge (+0.15, −0.05, −0.25 and −0.48 |e|). This symmetry phenomenon is the same as that for the M₂⊥gra structure in graphene that we studied [36]. The result that the metal atoms exhibit negative charges in the *h*-BN structure is also similar to previous results, which is mainly caused by the low electronegativity of the B atoms [40]. Concerning the magnetic properties, among the eight stable structures, all of them are ferromagnetic (FM), except for the Ni₂⊥vn-BN structure, which exhibits nonmagnetism (NM), and the Co₂⊥vb-BN structure, which exhibits antiferromagnetism (AFM), and the two metal atoms carry the same amount of magnetic moment, as shown in Table S2.

Meanwhile, we plotted the density of states (DOS) of the eight stable DACs (Figure S3). The DOS crosses the Fermi energy level for all of these DACs, indicating that all eight DACs have good conductivity and exhibit metallicity. This shows that the introduction of double metal atoms revolutionizes the wide band gap of *h*-BN and qualitatively improves the problem that the *h*-BN-loaded single-atom catalyst only narrows the original band gap of *h*-BN rather than completely converting it to metallicity [22,35], which is beneficial for electrocatalyzing the N₂ reduction reaction.

2.2. Screening of the DACs

NRR is a complicated reaction process involving different mechanisms, including distal [41], alternating [42] and enzymatic ones [43] (Figure 2). Among the proposed mechanisms, previous studies revealed that the first hydrogenation step ($*N_2 \rightarrow *N_2H$) is the potential-determining step (PDS) in most cases [44], mainly because of the high energy consumption during the first hydrogenation step due to the breakage of the inert $N \equiv N$ triple bond [45]. Therefore, we first used the free energy change in the first electronic step as screening criteria for the eight stable DACs. The free energy change ΔG in the first hydrogenation step ($*N_2 \rightarrow *N_2H$) is illustrated in Figure 3. For the end-on path, the free energy changes of the eight stable DACs all exceed 0.50 eV (the limiting potential $U_L = -0.5$ V on the surface of the mature catalyst Re(111) [46]); thus, the distal and alternating paths were not considered in our subsequent calculations. In contrast, the ΔG values of $*N_2 \rightarrow *N_2H$ over $Co_2 \perp vb-BN$, $Rh_2 \perp vb-BN$, $Pt_2 \perp vb-BN$ and $Rh_2 \perp vn-BN$ along the enzymatic path were 0.46, 0.50, 0.06 and 0.46 eV, respectively, and thus, these four DACs have the potential to be good NRR electrocatalysts based on the enzymatic route.

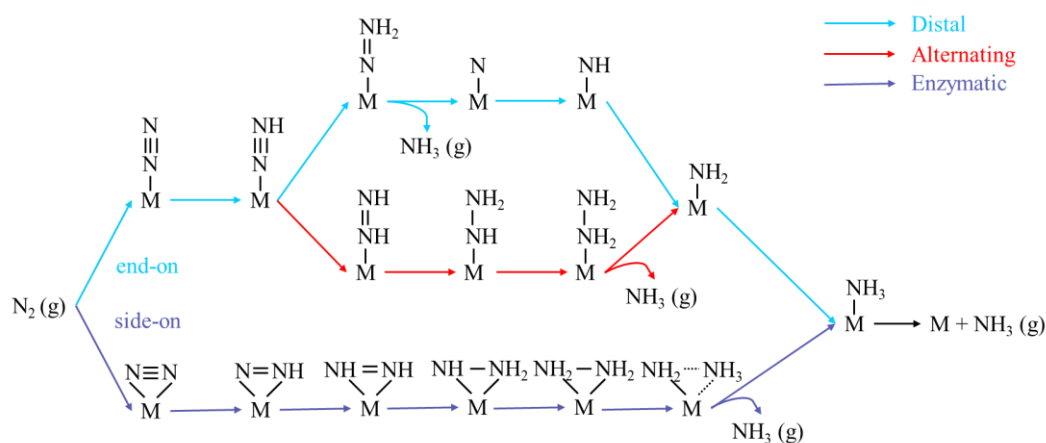


Figure 2. Three typical reaction pathways, including distal (blue), alternating (red) and enzymatic (dark blue) routes for NRR.

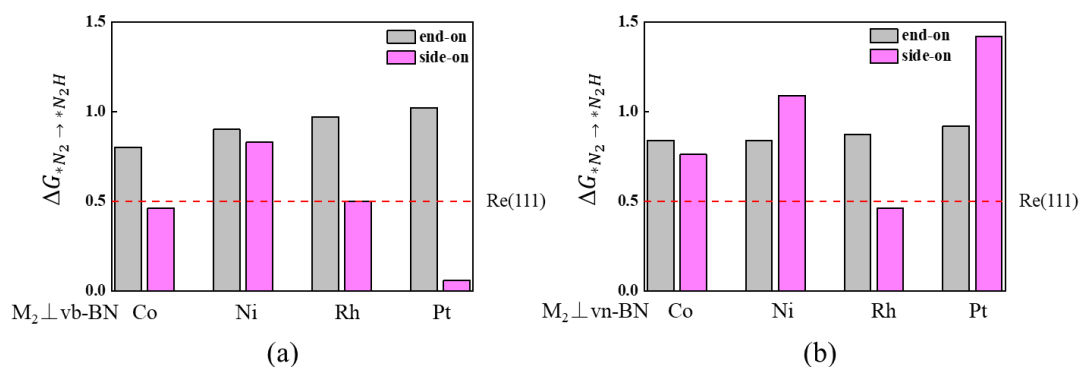


Figure 3. ΔG values of the first hydrogenation step ($*N_2 \rightarrow *N_2H$) over (a) $M_2 \perp vb-BN$ and (b) $M_2 \perp vn-BN$.

On the other hand, the suppression of the competitive hydrogenation reduction reaction (HER) is an essential feature required for a good NRR catalyst [44]. Therefore, we continued to use the effective inhibition of HER as another screening criterion for the four promising DACs: the free energy change $\Delta G(*N_2)$ of N_2 adsorption should be more negative than the intermediate $*H$'s value ($\Delta G(*H)$) [47]. Since the enzymatic path is favorable to proceed, as revealed in the above paragraph, we only compared the $\Delta G(*N_2)$ of the side-on adsorption conformation with that of H adsorption. The $\Delta G(*N_2)$ values are all more negative than $\Delta G(*H)$ on the four DACs (Figure S4), indicating that all four

DACs are able to restrain the HER reaction. Overall, $\text{Co}_2\perp\text{vb-BN}$, $\text{Rh}_2\perp\text{vb-BN}$, $\text{Pt}_2\perp\text{vb-BN}$ and $\text{Rh}_2\perp\text{vn-BN}$ were identified as potential NRR electrocatalysts through a two-step screening process.

2.3. The Reaction Pathway of NRR on Four Promising DACs

After screening the potential NRR catalysts ($\text{Co}_2\perp\text{vb-BN}$, $\text{Rh}_2\perp\text{vb-BN}$, $\text{Pt}_2\perp\text{vb-BN}$ and $\text{Rh}_2\perp\text{vn-BN}$), we started a specific study on their NRR catalytic activity. It is well known that N_2 adsorption on the catalyst surface is the first step in NRR, and its initial adsorption mode plays an important role in the subsequent reaction steps [22]. Based on the screening in Section 2.2, the distal and alternating paths are no longer applicable to these four DACs, so we focused on the side-on adsorption configurations corresponding to the enzymatic path; the optimized structures are displayed in Figure 4, and the adsorption energy and geometric parameters are given in Table S3. Actually, the N_2 molecules were not adsorbed exactly parallel to the BN sheet, except for $\text{Pt}_2\perp\text{vb-BN}$, but were slightly tilted, the same as in the previous study [22]. Compared to the free gas molecule, the bond length of the adsorbed N_2 molecule was stretched from 1.12 Å to 1.15~1.17 Å (Table S3). The adsorption energies calculated from Equation (2) (see Section 3) are all negative ($-1.26 \sim -0.89$ eV), indicating that N_2 adsorption on all four DACs is exothermic and that N_2 adsorption and activation on these DACs can easily occur at room temperature. Our Bader charge analysis shows that the electron transfer from the metal dimer to the adsorbed N_2 molecule is $-0.30 \sim -0.43$ |e| (Table S3), which is consistent with the results of the charge difference diagram (Figure S5). In conclusion, N_2 molecules can spontaneously adsorb on the four DACs and can be activated by these DACs for the subsequent reduction process.

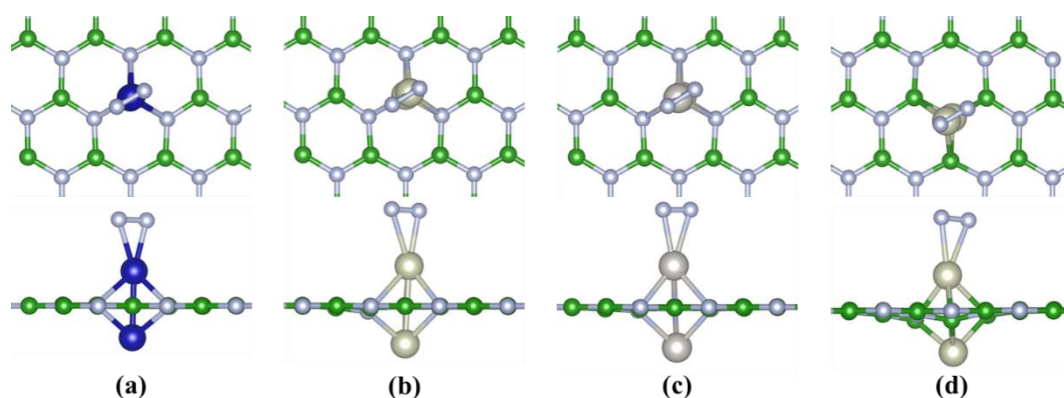


Figure 4. Optimized geometries of N_2 adsorption on (a) $\text{Co}_2\perp\text{vb-BN}$, (b) $\text{Rh}_2\perp\text{vb-BN}$, (c) $\text{Pt}_2\perp\text{vb-BN}$ and (d) $\text{Rh}_2\perp\text{vn-BN}$.

To evaluate the potential of the four DACs as electrocatalysts for converting N_2 to NH_3 , we calculated the free energy change of each elementary step along the enzymatic pathway over these DACs. The free energy corrections ($E_{ZPE} - TS$) for the free gas molecules used in the process are given in Table S4, and the free energy correction of each adsorbed species in the reaction pathways is listed in Table S5. When NRR follows the enzymatic pathway, protonation alternates between the two N atoms, releasing one ammonia molecule in the sixth electron step and one at the end, respectively (Figures 2 and 5). As for $\text{Co}_2\perp\text{vb-BN}$ (Figure 5a), in addition to the first hydrogenation step, there are two more steps, $^*\text{NNH} \rightarrow ^*\text{NHNH}$ and $^*\text{NHNH}_2 \rightarrow ^*\text{NH}_2\text{NH}_2$, in which the free energy change is raised, and the free energy change is 0.69 eV for the latter step, which is larger than 0.46 eV in the former step; thus, the potential-determining step (PDS) on $\text{Co}_2\perp\text{vb-BN}$ is $^*\text{NHNH}_2 \rightarrow ^*\text{NH}_2\text{NH}_2$. In contrast, for the other three DACs (Figure 5c,d), the PDS is the first hydrogenation step, since the corresponding ΔG is larger than those of other electron steps. It is noteworthy that during the reaction via the enzymatic mechanism over $\text{Pt}_2\perp\text{vb-BN}$ (Figure 5c), the free energy changes in the remaining five electron steps exhibit a successive

downhill trend, with only a slight increase in the free energy in the first electron step ($\Delta G = 0.06$ eV), which is very favorable for the reduction reaction to proceed.

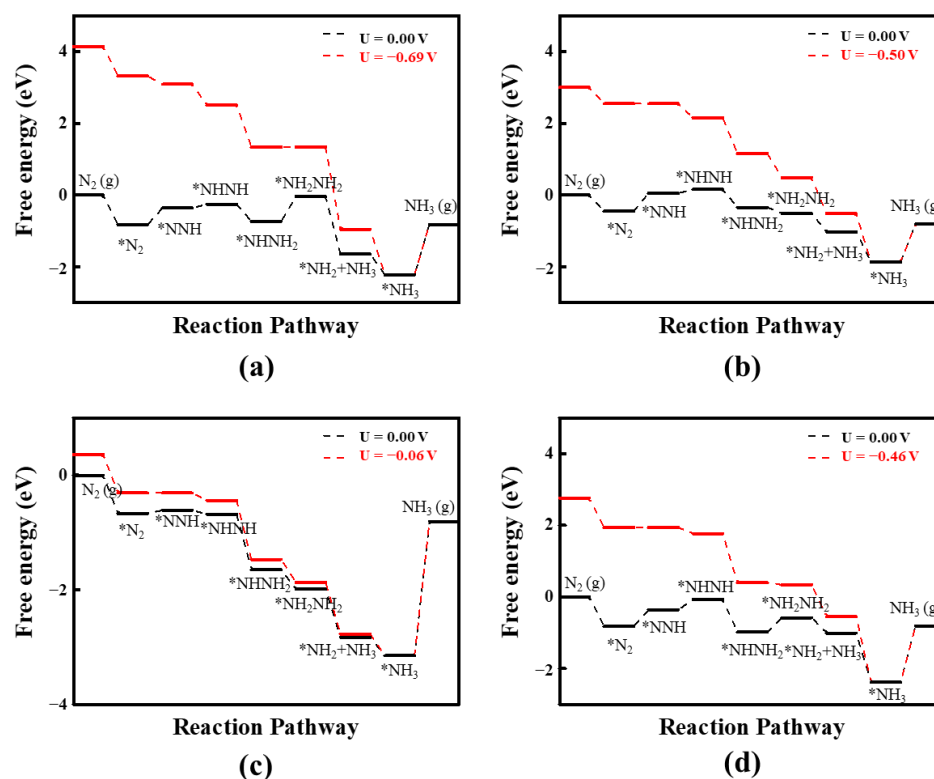


Figure 5. Free energy diagram of NRR on (a) $\text{Co}_2\perp\text{vb-BN}$, (b) $\text{Rh}_2\perp\text{vb-BN}$, (c) $\text{Pt}_2\perp\text{vb-BN}$ and (d) $\text{Rh}_2\perp\text{vn-BN}$ catalysts at zero and applied potentials (limiting potential) through the enzymatic mechanism.

The PDSs and limiting potentials (U_L) of the four DACs are presented in Table S6, and U_L is -0.69 V for $\text{Co}_2\perp\text{vb-BN}$, -0.50 V for $\text{Rh}_2\perp\text{vb-BN}$, -0.06 V for $\text{Pt}_2\perp\text{vb-BN}$ and -0.49 V for $\text{Rh}_2\perp\text{vn-BN}$. Our calculations indicate that the PDS of all three DACs except for $\text{Co}_2\perp\text{vb-BN}$ was the first electron step ($*\text{N}_2 \rightarrow *\text{NNH}$) (Table S6), which is a side note supporting that our use of the free energy change in the first electron step as a criterion for screening catalysts in Section 2.2 is reliable. In addition, three DACs ($\text{Rh}_2\perp\text{vb-BN}$, $\text{Pt}_2\perp\text{vb-BN}$ and $\text{Rh}_2\perp\text{vn-BN}$) have an absolute value of U_L less than 0.5 V, indicating that they are promising NRR catalysts (Table S6); in particular, $\text{Pt}_2\perp\text{vb-BN}$ has a very small U_L of -0.06 V, whose absolute value is much lower than those of the BN-supported SACs Mo-BN (-0.35 V) [22] and $\text{Mo-V}_{\text{N-BN}}$ (-0.24 V) [32].

In addition, we examined the NRR pathways on the single-atom catalysts (Rh@vb-BN , Pt@vb-BN and Rh@vn-BN in Figure S6) corresponding to the three DACs ($\text{Rh}_2\perp\text{vb-BN}$, $\text{Pt}_2\perp\text{vb-BN}$ and $\text{Rh}_2\perp\text{vn-BN}$) with good performance for comparison. Likewise, we considered the enzymatic pathway for the three SACs (Figure S7 and Table S6). According to Figure S7 and Table S6, the PDS for all three SACs is the first electron step ($*\text{N}_2 \rightarrow *\text{NNH}$), the same as the DACs; however, their ΔG values were much larger than the values of the DACs ($\text{Rh}_2\perp\text{vb-BN}/\text{Rh@vb-BN}$: 0.50/1.25 eV; $\text{Pt}_2\perp\text{vb-BN}/\text{Pt@vb-BN}$: 0.06/0.35 eV; and $\text{Rh}_2\perp\text{vn-BN}/\text{Rh@vn-BN}$: 0.49/1.48 eV). Moreover, the adsorption strength of N_2 on these three SACs is very weak, resulting in an increase in the free energies for adsorption when adding the corrections. Therefore, we believe that these three DACs with reverse sandwich structures have special potential as NRR electrocatalysts.

2.4. Origin of NRR Activity

To further investigate the origin of the activity of the four DACs with reverse sandwich structures, we examined the variation in atomic charge in each elementary step along the favorable enzymatic pathway (Figure 6). According to previous studies [22,37], each intermediate can be divided into three parts, namely, part 1 (BN sheet), part 2 (M_2 dimer) and part 3 (adsorbed N_xH_y species). Part 1 acts as an electron donor or acceptor, i.e., electron storage, during NRR, while part 2 acts as an emitter for electron transfer between part 3 and part 1, and our results have similar characteristics, with minimal electron changes on the M_2 dimer, which only acts as a “mediator” to transfer electrons, while the source and destination of the electrons gained and lost on the adsorbate is the BN monolayer. In the reaction path of the $Pt_2 \perp vb$ -BN catalyst with the best catalytic activity, the charge exchange between the BN monolayer and the adsorbed N_xH_y species is moderate among the four DACs, and the fifth electron step ($*NH_2NH_2 \rightarrow *NH_2 + NH_3$) with the largest charge exchange is more than $1 |e|$ (none of the other catalysts reach this value), indicating that the Pt_2 dimer plays a key role in the catalytic process to transfer electrons and improve the catalytic activity. In the $Rh_2 \perp vn$ -BN catalyst, the overall charge transfer and fluctuations are smaller than those of the other three catalysts with metal bonded to N atoms, because the Rh atoms bonded with B atoms seize electrons from B and show negative charges.

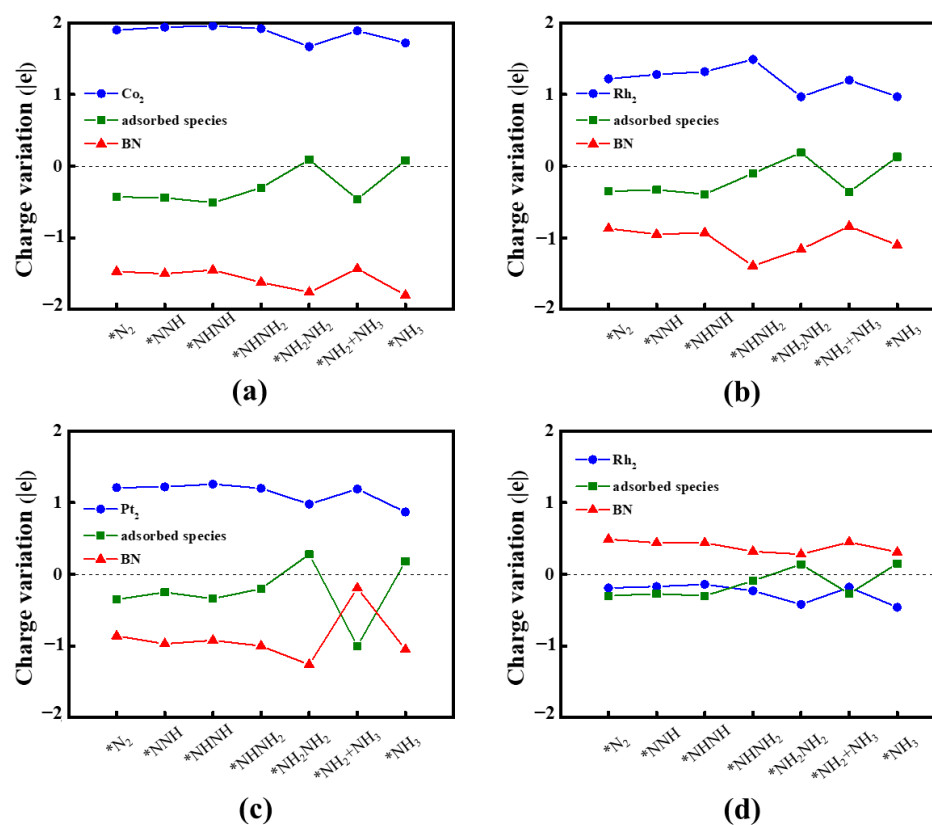


Figure 6. Charge variation of the three moieties along the enzymatic pathway on (a) $Co_2 \perp vb$ -BN, (b) $Rh_2 \perp vb$ -BN, (c) $Pt_2 \perp vb$ -BN and (d) $Rh_2 \perp vn$ -BN.

Furthermore, we calculated the projected density of states (PDOS) of the four DACs with the adsorption of N_2 . As shown in Figure S8, compared to the free N_2 molecule, all four DACs provide electrons to the $2\pi^*$ orbitals above the Fermi energy level, bringing them down from above 5 eV to near the Fermi energy level, and the d orbitals of the metals are well coupled to the $2\pi^*$ orbitals. Among them, the d orbitals of $Pt_2 \perp vb$ -BN not only have good hybridization with the $2\pi^*$ and $3\sigma^*$ orbitals of the N_2 molecule but also couple well with the 2π and 3σ orbitals below the Fermi energy level, which might be associated with $Pt_2 \perp vb$ -BN's superior performance.

Considering the distinguished catalytic performance of Pt₂⊥vb-BN towards NRR, we assessed the feasibility of synthesizing the inverse sandwich structure of Pt₂⊥vb-BN in the experiment by immersing defective graphene in a PtCl₂ aqueous solution and performing an FPMD simulation in the NVT ensemble at 400 K; such a strategy was proposed previously [48,49]. The formation of the inverse sandwich structure occurred at about 0.5 ps of the FPMD simulation (Figure S9), indicating the feasibility of the experimental realization of our novel DAC model.

3. Computational Methods

In this work, spin-polarized density function theory (DFT) calculations were performed using the Vienna Ab initio Simulation Package (VASP) [50,51]. The Perdew–Burke–Ernzerhof (PBE) functional within the generalized gradient approximation (GGA) was utilized to describe the exchange–correlation energy [52]. The projector augmented-wave (PAW) method was used to describe the interactions between ion cores and valence electrons [53]. The Brillouin zone was sampled by the Monkhorst–Pack (MP) scheme and $3 \times 3 \times 1$ k points [35]. The kinetic energy cutoff for the plane-wave basis set was chosen to be 600 eV. The van der Waals (vdW) interactions between the reactants/intermediates and the catalyst were considered using the DFT-D2 method [54]. The force on each atom in the self-consistent iteration was 0.001 eV/Å, and the energy convergence criterion was 1×10^{-6} eV. The Poisson–Boltzmann implicit solvation model with a dielectric constant of $\epsilon = 80$ for water was used to simulate the H₂O solvent environment [55]. Bader charge analysis was adopted to evaluate the charge transfer [56].

First-principles molecular dynamics (FPMD) simulations were carried out to assess the thermal stability of the structures. The temperature was controlled by the Nosé–Hoover method [57]. The material was annealed at a room temperature of 300 K. Each FPMD simulation in the NVT ensemble lasted 5 ps with a time step of 1 fs.

To model M₂⊥vb-BN and M₂⊥vn-BN, we used a 5×5 *h*-BN supercell in our calculations (Figure 1). One boron atom or one nitrogen atom in the center of the *h*-BN supercell was removed to form a vacancy defect, denoted as vb-BN and vn-BN, respectively, and then the transition-metal atoms were symmetrically positioned above and below the vacancy, respectively, to form an inverse sandwich structure, where the M₂ dimer was perpendicular to the *h*-BN plane. A vacuum space of 15 Å in the direction perpendicular to the BN plane was applied to avoid image interactions [58].

The binding energy (E_b) per M atom on defective graphene was defined as:

$$E_b = (E_{M_2 \perp vx-BN} - E_{vx-BN} - 2E_M) / 2 \quad (1)$$

where $E_{M_2 \perp vx-BN}$ ($x = b$ or n) is the total energy of the M₂⊥vb-BN or M₂⊥vn-BN structure, and E_{vx-BN} ($x = b$ or n) and E_M refer to the energies of the defective *h*-BN and a free M atom, respectively. According to the definition, a more negative E_b value indicates a stronger binding strength between the metal atoms and the BN substrate.

The adsorption energy (E_{ad}) of reaction intermediates can be obtained from the following formula:

$$E_{ad} = E_{total} - E_{catalyst} - E_{adsorbate} \quad (2)$$

where E_{total} , $E_{catalyst}$ and $E_{adsorbate}$ are the energies of the adsorbate-adsorbed catalyst, the bare catalyst and the free adsorbate, respectively [59]. By this definition, a positive/negative value of E_{ad} indicates that the adsorption is endothermic/exothermic.

The free energy (G) of each intermediate is given by:

$$G = E_{DFT} + E_{ZPE} - TS \quad (3)$$

where E_{DFT} is the energy from the DFT calculation, and E_{ZPE} and TS are the zero-point energy and entropy corrections, respectively [35]. The corrections for E_{ZPE} and S can be obtained from vibration frequency calculations [60], and T is the temperature (298.15 K).

The free energy G for each step in the whole NRR was calculated according to the computational hydrogen electrode (CHE) model proposed by Nørskov and coworkers [61]. According to the CHE model, the effect of the electrode potential (U) and pH on NRR

can be considered an energy shift of the free energy change in the electrochemical step: $\Delta G_U = -eU$; $\Delta G_{pH} = -k_B T \ln 10 \times pH$, where k_B is the Boltzmann constant, and pH was set as zero in this study to mimic the strong acidic condition. The limiting potential (U_L) is defined as the maximum free energy change (ΔG_{max}) among all elementary steps along the most favorable pathway: $U_L = -\Delta G_{max}/e$ [22,62].

4. Conclusions

In conclusion, we screened the NRR activity of 10 DACs with inverse sandwich structures, $M_2 \perp vb$ -BN ($M = Co, Ni, Rh, Ir$ and Pt) and $M_2 \perp vn$ -BN ($M = Co, Ni, Rh, Ir$ and Pt), by comprehensive DFT calculations. After a stability evaluation and an initial screening of two conditions (moderate ΔG for the first hydrogenation step and the effective suppression of HER), we identified four potential DACs; then, through complete enzymatic pathway calculations, three DACs ($Rh_2 \perp vb$ -BN, $Pt_2 \perp vb$ -BN and $Rh_2 \perp vn$ -BN) with good NRR activity were identified. Notably, $Pt_2 \perp vb$ -BN has a limiting potential of only -0.06 V, which is superior to many reported NRR electrocatalysts. The activity of the DACs with inverse sandwich structures was compared with the corresponding three SACs, and the electrocatalytic performance of the DACs with inverse sandwich structures was found to prevail over that of their corresponding SAC counterparts. Thus, our calculations demonstrate that three stable DACs with inverse sandwich structures are promising NRR electrocatalysts, echoing our recent work showing that vertical metal dimers can be anchored in suitable 2D materials, not limited to graphene, and DACs with such inverse sandwich structures may be used for CO_2RR and beyond [37]. We hope that our proposed double-atom catalysts featuring inverse sandwich structures will stimulate experimental and theoretical studies to further explore their variation and potential in electrocatalysis.

Supplementary Materials: The following Supporting Information can be downloaded at: <https://www.mdpi.com/article/10.3390/catal12111387/s1>. Table S1: The distance between metal atoms, the binding energies of metal atoms in 10 species, the cohesive energies of bulk M and $E_b - E_{coh}$; Table S2: The Bader charge on M atoms, the magnetic order and the magnetic moment on M atoms of the stable catalyst structures; Table S3: The adsorption energy, the charge transferred from the stable DACs to the adsorbed N_2 , the shortest distance between N_2 and M , and the distance between the N atom and N atom in N_2 of the N_2 molecule adsorbed on the stable catalyst structures; Table S4: The $E_{zpe} - TS$ of the free gas molecules; Table S5: Free energy correction ($E_{zpe} - TS$) for each adsorbed species in the NRR reaction path on $Co_2 \perp vb$ -BN, $Rh_2 \perp vb$ -BN, $Pt_2 \perp vb$ -BN and $Rh_2 \perp vn$ -BN; Table S6: The potential-determining steps and limiting potentials for NRR on the stable catalyst structures; Figure S1: Structural diagram of the single-cell structures of (a) h -BN, (b) vb -BN and (c) vn -BN models. Color scheme: B, green; N, silver; Figure S2: The energy evolution of the eight DACs during 5 ps FPMD simulations at 300 K; the insets are the final annealed structures; Figure S3: Density of states (DOS) of the eight DACs; Figure S4: Calculated $\Delta G(*N_2)$ and $\Delta G(*H)$ on the four promising DACs; Figure S5: Differential charge diagram of N_2 adsorbed on (a) $Co_2 \perp vb$ -BN, (b) $Rh_2 \perp vb$ -BN, (c) $Pt_2 \perp vb$ -BN and (d) $Rh_2 \perp vn$ -BN; Figure S6: Structural diagram of the (a) $M@vb$ -BN and (b) $M@vn$ -BN models; Figure S7: Free energy diagram of NRR on (a) $Rh@vb$ -BN, (b) $Pt@vb$ -BN and $Rh@vn$ -BN catalysts at zero and applied potentials (limiting potential) through the enzymatic mechanism; Figure S8: The projected density of states (PDOS) for (a) $Co_2 \perp vb$ -BN, (b) $Rh_2 \perp vb$ -BN, (c) $Pt_2 \perp vb$ -BN and (d) $Rh_2 \perp vn$ -BN; Figure S9: Top and side views of the snapshots of atomic configurations of FAMD simulations for the synthetic process of $Pt_2 \perp vb$ -BN.

Author Contributions: F.L. outlined the work plan; L.Y. conducted the computations, drew the figures and drafted the manuscript. All authors participated in the review and publication processes of the article. All authors have read and agreed to the published version of the manuscript.

Funding: This work was funded by the National Natural Science Foundation of China (11704203 and 11964024), the "Grassland Talents" project of the Inner Mongolia Autonomous Region (12000-12102613), and the Young Science and Technology Talents Cultivation Project of Inner Mongolia University (21200-5223708).

Data Availability Statement: Not applicable.

Acknowledgments: The authors are grateful for the computational support from Beijing PARATERA.

Conflicts of Interest: The authors declare no conflict of interest.

References

1. Zhang, H.; Xu, G.; Zhang, L.; Wang, W.; Miao, W.; Chen, K.; Cheng, L.; Li, Y.; Han, S. Ultrafine cobalt nanoparticles supported on carbon nanospheres for hydrolysis of sodium borohydride. *Renew. Energy* **2020**, *162*, 345–354. [[CrossRef](#)]
2. Rapson, T.D.; Gregg, C.M.; Allen, R.S.; Ju, H.; Doherty, C.M.; Mulet, X.; Giddey, S.; Wood, C.C. Insights into nitrogenase bioelectrocatalysis for green ammonia production. *ChemSusChem* **2020**, *13*, 4856–4865. [[CrossRef](#)] [[PubMed](#)]
3. Karl, D.; Letelier, R.; Tupas, L.; Dore, J.; Christian, J.; Hebel, D. The role of nitrogen fixation in biogeochemical cycling in the subtropical north pacific ocean. *Nature* **1997**, *388*, 533. [[CrossRef](#)]
4. Hoffman, B.M.; Lukoyanov, D.; Yang, Z.-Y.; Dean, D.R.; Seefeldt, L.C. Mechanism of nitrogen fixation by nitrogenase: The next stage. *Chem. Rev.* **2014**, *114*, 4041–4062. [[CrossRef](#)]
5. Guo, X.; Gu, J.; Lin, S.; Zhang, S.; Chen, Z.; Huang, S. Tackling the activity and selectivity challenges of electrocatalysts toward the nitrogen reduction reaction via atomically dispersed biatom catalysts. *J. Am. Chem. Soc.* **2020**, *142*, 5709–5721. [[CrossRef](#)]
6. Zhang, X.; Chen, A.; Zhang, Z.; Zhou, Z. Double-atom catalysts: Transition metal dimeranchored C₂N monolayers as N₂ fixation electrocatalysts. *J. Mater. Chem. A* **2018**, *6*, 18599–18604. [[CrossRef](#)]
7. Erisman, J.W.; Sutton, M.A.; Galloway, J.; Klimont, Z.; Winiwarter, W. How a century of ammonia synthesis changed the world. *Nat. Geosci.* **2008**, *1*, 636. [[CrossRef](#)]
8. Ferrara, M.; Melchionna, M.; Fornasiero, P.; Bevilacqua, M. The role of structured carbon in downsized transition metal-based electrocatalysts toward a green nitrogen fixation. *Catalysts* **2021**, *11*, 1529. [[CrossRef](#)]
9. Ham, C.J.M.; Koper, M.T.M.; Hetterscheid, D.G.H. Challenges in reduction of dinitrogen by proton and electron transfer. *Chem. Soc. Rev.* **2014**, *43*, 5183–5191.
10. Tanabe, Y.; Nishibayashi, Y. Developing more sustainable processes for ammonia synthesis. *Coord. Chem. Rev.* **2013**, *257*, 2551–2564. [[CrossRef](#)]
11. Wang, S.; Ichihara, F.; Pang, H.; Chen, H.; Ye, J. Nitrogen fixation reaction derived from nanostructured catalytic materials. *Adv. Funct. Mater.* **2018**, *28*, 1803309. [[CrossRef](#)]
12. Kyriakou, V.; Garagounis, I.; Vasileiou, E.; Vourros, A.; Stoukides, M. Progress in the electrochemical synthesis of ammonia. *Catal. Today* **2017**, *286*, 2–13. [[CrossRef](#)]
13. Liu, X.; Jiao, Y.; Zheng, Y.; Qiao, S.-Z. Isolated boron sites for electroreduction of dinitrogen to ammonia. *ACS Catal.* **2020**, *10*, 1847–1854. [[CrossRef](#)]
14. Li, L.; Tang, C.; Xia, B.; Jin, H.; Zheng, Y.; Qiao, S.-Z. Two-dimensional mosaic bismuth nanosheets for highly selective ambient electrocatalytic nitrogen reduction. *ACS Catal.* **2019**, *9*, 2902–2908. [[CrossRef](#)]
15. Yan, Z.; Ji, M.; Xia, J.; Zhu, H. Recent advanced materials for electrochemical and photoelectrochemical synthesis of ammonia from dinitrogen: One step closer to a sustainable energy future. *Adv. Energy Mater.* **2020**, *10*, 1902020. [[CrossRef](#)]
16. Qiao, B.; Wang, A.; Yang, X.; Allard, L.F.; Jiang, Z.; Cui, Y.; Liu, J.; Li, J.; Zhang, T. Single-atom catalysis of CO oxidation using Pt₁/FeO_x. *Nat. Chem.* **2011**, *3*, 634–641. [[CrossRef](#)]
17. Jeong, H.; Shin, S.; Lee, H. Heterogeneous atomic catalysts overcoming the limitations of single-atom catalysts. *ACS Nano* **2020**, *14*, 14355–14374. [[CrossRef](#)] [[PubMed](#)]
18. Yu, L.; Li, F.; Zhao, J.; Chen, Z. Revisiting catalytic performance of supported metal dimers for oxygen reduction reaction via magnetic coupling from first principles. *Adv. Powder Mater.* **2022**, *1*, 100031. [[CrossRef](#)]
19. Zhang, S.; Wu, Y.; Zhang, Y.-X.; Niu, Z. Dual-atom catalysts: Controllable synthesis and electrocatalytic applications. *Sci. China Chem.* **2021**, *64*, 1908–1922. [[CrossRef](#)]
20. Lü, F.; Zhao, S.; Guo, R.; He, J.; Peng, X.; Bao, H.; Fu, J.; Han, L.; Qi, G.; Luo, J.; et al. Nitrogen-coordinated single Fe sites for efficient electrocatalytic N₂ fixation in neutral media. *Nano Energy* **2019**, *61*, 420–427. [[CrossRef](#)]
21. Yin, H.; Li, S.-L.; Gan, L.-Y.; Wang, P. Pt-embedded in monolayer g-C₃N₄ as a promising single-atom electrocatalyst for ammonia synthesis. *J. Mater. Chem. A* **2019**, *7*, 11908–11914. [[CrossRef](#)]
22. Zhao, J.; Chen, Z. Single Mo atom supported on defective boron nitride monolayer as an efficient electrocatalyst for nitrogen fixation: A computational study. *J. Am. Chem. Soc.* **2017**, *139*, 12480–12487. [[CrossRef](#)] [[PubMed](#)]
23. Han, B.; Meng, H.; Li, F.; Zhao, J. Fe₃ cluster anchored on the C₂N monolayer for efficient electrochemical nitrogen fixation. *Catalysts* **2020**, *10*, 974. [[CrossRef](#)]
24. Arachchige, L.J.; Xu, Y.; Dai, Z.; Zhang, X.; Wang, F.; Sun, C. Theoretical investigation of single and double transition metals anchored on graphene monolayer for nitrogen reduction reaction. *J. Phys. Chem. C* **2020**, *124*, 15295–15301. [[CrossRef](#)]
25. Ma, L.; Zeng, X.C. Catalytic directional cutting of hexagonal boron nitride: The roles of interface and etching agents. *Nano Lett.* **2017**, *17*, 3208–3214. [[CrossRef](#)]
26. Xu, D.; Liu, Y.; Zhao, J.; Cai, Q.; Wang, X. Theoretical study of the deposition of Pt clusters on defective hexagonal boron nitride (*h*-BN) sheets: Morphologies, electronic structures, and interactions with O. *J. Phys. Chem. C* **2014**, *118*, 8868–8876. [[CrossRef](#)]

27. Lin, Y.; Bunker, C.E.; Fernando, K.A.S.; Connell, J.W. Aqueously dispersed silver nanoparticle-decorated boron nitride nanosheets for reusable, Thermal oxidation-resistant surface enhanced raman spectroscopy (SERS) devices. *ACS Appl. Mater. Interfaces* **2012**, *4*, 1110–1117. [[CrossRef](#)]
28. Cao, L.; Dai, P.; Tang, J.; Li, D.; Chen, R.; Liu, D.; Gu, X.; Li, L.; Bando, Y.; Ok, Y.S.; et al. Spherical superstructure of boron nitride nanosheets derived from boron-containing metal-organic frameworks. *J. Am. Chem. Soc.* **2020**, *142*, 8755–8762. [[CrossRef](#)]
29. Xiong, J.; Di, J.; Zhu, W.; Li, H. Hexagonal boron nitride adsorbent: Synthesis, performance tailoring and applications. *J. Energy Chem.* **2020**, *40*, 99–111. [[CrossRef](#)]
30. Deng, C.; He, R.; Shen, W.; Li, M. Theoretical analysis of oxygen reduction reaction activity on single metal (Ni, Pd, Pt, Cu, Ag, Au) atom supported on defective two-dimensional boron nitride materials. *Phys. Chem. Chem. Phys.* **2019**, *21*, 18589–18594. [[CrossRef](#)]
31. Deng, C.; He, R.; Shen, W.; Li, M.; Zhang, T. A single-atom catalyst of cobalt supported on a defective two-dimensional boron nitride material as a promising electrocatalyst for the oxygen reduction reaction: A DFT study. *Phys. Chem. Chem. Phys.* **2019**, *21*, 6900–6907. [[CrossRef](#)] [[PubMed](#)]
32. Zhang, L.; Meng, Y.; Koso, A.; Yao, Y.; Tang, H.; Xia, S. The mechanism of nitrogen reduction reaction on defective boron nitride (BN) monolayer doped with monatomic Co, Ni, and Mo—A first principles study. *Colloid. Surf. A* **2022**, *647*, 129072. [[CrossRef](#)]
33. Huang, B.; Wu, Y.; Luo, Y.; Zhou, N. Double atom-anchored defective boron nitride catalyst for efficient electroreduction of CO₂ to CH₄: A first principles study. *Chem. Phys. Lett.* **2020**, *756*, 137852. [[CrossRef](#)]
34. Cui, Q.; Qin, G.; Wang, W.; Sun, L.; Du, A.; Sun, Q. Mo-doped boron nitride monolayer as a promising single-atom electrocatalyst for CO₂ conversion. *Beilstein J. Nanotechnol.* **2019**, *10*, 540–548. [[CrossRef](#)]
35. Wang, S.; Xin, Y.; Yuan, J.; Wang, L.; Zhang, W. Direct conversion of methane to methanol on boron nitride-supported copper single atoms. *Nanoscale* **2022**, *14*, 5447–5453. [[CrossRef](#)]
36. Yu, L.; Li, F. Metal dimers embedded vertically in defectgraphene as gas sensors: A first-principles study. *Phys. Chem. Chem. Phys.* **2022**, *24*, 9842–9847. [[CrossRef](#)]
37. Yu, L.; Li, F.; Huang, J.; Sumpter, B.G.; Mustain, W.E.; Chen, Z. Double-atom catalysts featuring inverse sandwich structure for CO₂ reduction reaction: A synergetic first-principles and machine learning investigation. *Adv. Funct. Mater.* **2022**; under review.
38. Si, M.S.; Xue, D.S. Magnetic properties of vacancies in a graphitic boron nitride sheet by first-principles pseudopotential calculations. *Phys. Rev. B* **2007**, *75*, 193409. [[CrossRef](#)]
39. Zeng, H.; Liu, X.; Chen, F.; Chen, Z.; Fan, X.; Lau, W. Single atoms on a nitrogen-doped boron phosphide monolayer: A new promising bifunctional electrocatalyst for ORR and OER. *ACS Appl. Mater. Interfaces* **2020**, *12*, 52549–52559. [[CrossRef](#)]
40. Ali, S.; Haneef, M.; Akbar, J.; Ullah, I.; Ullah, S.; Samad, A. Single Au atom supported defect mediated boron nitride monolayer as an efficient catalyst for acetylene hydrochlorination: A first principles study. *Mol. Catal.* **2021**, *511*, 111753. [[CrossRef](#)]
41. Chatt, J.; Dilworth, J.R.; Richards, R.L. Recent advances in the chemistry of nitrogen fixation. *Chem. Rev.* **1978**, *78*, 589–625. [[CrossRef](#)]
42. Seefeldt, L.C.; Hoffman, B.M.; Dean, D.R. Mechanism of Mo-dependent nitrogenase. *Annu. Rev. Biochem.* **2009**, *78*, 701–722. [[CrossRef](#)] [[PubMed](#)]
43. Hinnemann, B.; Nørskov, J.K. Catalysis by enzymes: The biological ammonia synthesis. *Top. Catal.* **2006**, *37*, 55–70. [[CrossRef](#)]
44. Zheng, G.; Li, L.; Hao, S.; Zhang, X.; Tian, Z.; Chen, L. Double atom catalysts: Heteronuclear transition metal dimer anchored on nitrogen-doped graphene as superior electrocatalyst for nitrogen reduction reaction. *Adv. Theory Simul.* **2020**, *3*, 2000190. [[CrossRef](#)]
45. Zheng, G.; Li, L.; Tian, Z.; Zhang, X.; Chen, L. Heterogeneous single-cluster catalysts (Mn₃, Fe₃, Co₃, and Mo₃) supported on nitrogen-doped graphene for robust electrochemical nitrogen reduction. *J. Energy Chem.* **2021**, *54*, 612–619. [[CrossRef](#)]
46. Montoya, J.H.; Tsai, C.; Vojvodic, A.; Nørskov, J.K. The challenge of electrochemical ammonia synthesis: A new perspective on the role of nitrogen scaling relations. *ChemSusChem* **2015**, *8*, 2180–2186. [[CrossRef](#)] [[PubMed](#)]
47. Choi, C.; Back, S.; Kim, N.-Y.; Lim, J.; Kim, Y.-H.; Jung, Y. Suppression of hydrogen evolution reaction in electrochemical N₂ reduction using single-atom catalysts: A computational guideline. *ACS Catal.* **2018**, *8*, 7517–7525. [[CrossRef](#)]
48. Ling, C.; Shi, L.; Ouyang, Y.; Zeng, X.C.; Wang, J. Nanosheet supported single-metal atom bifunctional catalyst for overall water splitting. *Nano Lett.* **2017**, *17*, 5133–5139. [[CrossRef](#)]
49. Li, F.; Liu, X.; Chen, Z. 1+1' > 2: Heteronuclear bi-atom catalyst outperforms its homonuclear counterparts for CO oxidation. *Small Methods* **2019**, *3*, 1800480. [[CrossRef](#)]
50. Kresse, G.G.; Furthmüller, J.J. Efficient iterative schemes for ab initio total-energy calculations using a plane-wave basis set. *Phys. Rev. B* **1996**, *54*, 11169–11186. [[CrossRef](#)]
51. Kresse, G.G.; Furthmüller, J.J. Efficiency of ab-initio total energy calculations for metals and semiconductors using a plane-wave basis set. *Comput. Mater. Sci.* **1996**, *6*, 15–50.
52. Perdew, J.P.; Burke, K.; Ernzerhof, M. Generalized gradient approximation made simple. *Phys. Rev. Lett.* **1996**, *77*, 3865–3868. [[CrossRef](#)] [[PubMed](#)]
53. Blöchl, P.E. Projector augmented-wave method. *Phys. Rev. B* **1994**, *50*, 17953–17979. [[CrossRef](#)] [[PubMed](#)]
54. Bučko, T.; Hafner, J.; Lebègue, S.; Ángyán, J.G. Improved description of the structure of molecular and layered crystals: Ab initio DFT calculations with van der Waals corrections. *J. Phys. Chem. A* **2010**, *114*, 11814–11824. [[CrossRef](#)] [[PubMed](#)]

55. Mathew, K.; Sundararaman, R.; Letchworth-Weaver, K.; Arias, T.A.; Hennig, R.G. Implicit solvation model for density-functional study of nanocrystal surfaces and reaction pathways. *J. Chem. Phys.* **2014**, *140*, 084106. [[CrossRef](#)] [[PubMed](#)]
56. Henkelman, G.; Arnaldsson, A.; Jónsson, H. A fast and robust algorithm for Bader decomposition of charge density. *Comput. Mater. Sci.* **2006**, *36*, 354–360. [[CrossRef](#)]
57. Martyna, G.J.; Klein, M.L.; Tuckerman, M.E. Nose–Hoover chains: The canonical ensemble via continuous dynamics. *J. Chem. Phys.* **1992**, *97*, 2635. [[CrossRef](#)]
58. Impeng, S.; Junkaew, A.; Maitarad, P.; Kungwan, N.; Zhang, D.; Shi, L.; Namuangruk, S. A MnN₄ moiety embedded graphene as a magnetic gas sensor for CO detection: A first principle study. *Appl. Surf. Sci.* **2019**, *473*, 820–827. [[CrossRef](#)]
59. Fu, L.; Wang, R.; Zhao, C.; Huo, J.; He, C.; Kim, K.-H.; Zhang, W. Construction of Cr-embedded graphyne electrocatalyst for highly selective reduction of CO₂ to CH₄: A DFT study. *Chem. Eng. J.* **2021**, *414*, 128857. [[CrossRef](#)]
60. Ling, C.; Zhang, Y.; Li, Q.; Bai, X.; Shi, L.; Wang, J. New mechanism for N₂ reduction: The essential role of surface hydrogenation. *J. Am. Chem. Soc.* **2019**, *141*, 18264–18270. [[CrossRef](#)]
61. Nørskov, J.K.; Rossmeisl, J.; Logadottir, A.; Lindqvist, L. Origin of the overpotential for oxygen reduction at a fuel-cell cathode. *J. Phys. Chem. B* **2004**, *108*, 17886–17892. [[CrossRef](#)]
62. Skulason, E.; Bligaard, T.; Gudmundsdottir, S.; Studt, F.; Rossmeisl, J.; Abild-Pedersen, F.; Vegge, T.; Jonssonac, H.; Nørskov, J.K. A theoretical evaluation of possible transition metal electro-catalysts for N₂ reduction. *Phys. Chem. Chem. Phys.* **2012**, *14*, 1235–1245. [[CrossRef](#)] [[PubMed](#)]